

Formation of Temporally Shaped Electron Bunches for Beam-Driven Collinear Wakefield Accelerators

Wei Hou Tan,^{1,*} Philippe Piot,^{1,2} and Alexander Zholents²

¹*Northern Illinois Center for Accelerator & Detector Development and Department of Physics,
Northern Illinois University, DeKalb, IL 60115, USA*

²*Argonne National Laboratory, Lemont, IL 60439, USA*

(Dated: November 21, 2021)

Beam-driven collinear wakefield accelerators (CWAs) that operate by using slow-wave structures or plasmas hold great promise toward reducing the size of contemporary accelerators. Sustainable acceleration of charged particles to high energies in the CWA relies on using field-generating relativistic electron bunches with a highly asymmetric peak current profile and a large energy chirp. A new approach to obtaining such bunches has been proposed and illustrated with the accelerator design supported by particle tracking simulations. It has been shown that the required particle distribution in the longitudinal phase space can be obtained without collimators, giving CWAs an opportunity for employment in applications requiring a high repetition rate of operation.

PACS numbers: 29.27.-a, 41.85.-p, 41.75.Fr

I. INTRODUCTION

In a beam-based collinear wakefield accelerator (CWA), a high-charge drive bunch generates an electromagnetic field passing through a slow-wave structure (a dielectric-lined or corrugated waveguide) or plasma. This field, called the wakefield, is used to accelerate a witness bunch propagating the structure in the same direction behind the drive bunch [1–8]. An important figure of merit for a CWA is the transformer ratio, $\mathcal{R} \equiv |\mathcal{E}_+/\mathcal{E}_-|$, where \mathcal{E}_+ is the maximum accelerating field behind the drive bunch, and \mathcal{E}_- is the maximum decelerating field within the drive bunch. For symmetric drive-bunch current distribution in time $I(t)$, the transformer ratio is limited to $\mathcal{R} < 2$ [9]. However, asymmetric $I(t)$ can significantly enhance the transformer ratio [9], albeit at the expense of reduced \mathcal{E}_+ and \mathcal{E}_- [10].

Bunch-shaping techniques investigated hitherto are photocathode-laser intensity shaping [11–13], transverse-to-longitudinal phase-space exchange [14–16], and use of multi-frequency linacs [17]. Despite significant progress, they suffer either from their inability to deliver highly asymmetric bunches or from prohibitively large beam losses on collimators. Consequently, producing drive bunches with an asymmetric peak current profile while preserving most of the bunch electrons has been an active research topic.

Another important consideration for a drive bunch arises from its proneness to the transverse beam-break-up (BBU) instability caused by the strong transverse forces due to the transverse wakefield [18–20]. A possible BBU-mitigation technique consists of imparting a large energy chirp along the drive bunch [21–23] and creating a current profile $I(t)$ that stimulates a dynamic adjustment of this chirp concurrently with the wakefield-induced bunch

deceleration in the CWA [24].

The work reported in this paper was motivated by a design of a high repetition rate CWA for use in a free-electron laser (FEL) facility described in Refs. [25, 26]. This facility plans to employ up to ten FELs individually driven by a dedicated CWA. A single conventional accelerator delivers ~ 1 GeV drive electron bunches with a highly asymmetric $I(t)$ and a large energy chirp to the ten CWAs. Since the drive-bunch charge considered in [25, 26] is up to 10 nC and the bunch repetition rate up to 500 kHz, the electron beam carries significant power. Therefore, using collimators to assist with the bunch shaping is prohibitive, and, consequently, preparing the drive bunches doing otherwise becomes a prime challenge.

To solve the problem, we undertook a new approach and distributed the task of obtaining the highly asymmetric $I(t)$ over the entire drive bunch accelerator beginning from the photocathode electron gun and ending by the final bunch compressor. To the best of our knowledge, our work demonstrates for the first time a pathway to obtaining electron bunches with a highly asymmetric $I(t)$, avoiding prohibitively large electron losses on collimators. The employed technique is rather generic and can be used for preparing the electron bunch peak current distribution with profiles different than those considered in this paper.

Although the main focus of the work was to obtain a drive bunch with the required distribution in the longitudinal phase space (LPS), an equally important additional objective, was to ensure the associated transverse emittances commensurate with the small CWA aperture.

II. THE DRIVE BUNCH AND THE WAKEFIELD

We define the longitudinal charge distribution in the electron bunch as $q(z)$ and consider bunches localized on

* wtan1@niu.edu

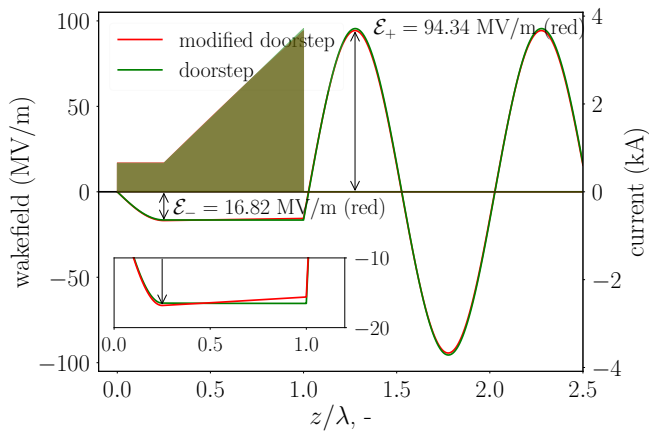


Figure 1. Nominal (green trace) and modified doorstep distributions with associated wakefields calculated using $L = \lambda$, $\chi = 0$ and $\chi = -\frac{1}{10\lambda}$, respectively. The wakefields are computed for a bunch charge of 10 nC and use a single-mode Green's function, where $f = 180$ GHz and $\kappa_{\parallel} = 14.3$ kV/pC/m calculated using ECHO[30]. The transformer ratio for the modified doorstep distribution shown in the plot is $\mathcal{R} = 5.6$.

the interval $0 \leq z \leq L$, where z is the distance behind the bunch head. Therefore, we have

$$\int_0^L q(z) dz = Q, \quad (1)$$

where Q is the total bunch charge. Following [10], we use the Green's function $G(z)$ consisting only of a fundamental mode $G(z) = 2\kappa_{\parallel} \cos(kz)H(z)$ ¹, where κ_{\parallel} is the loss factor of a point particle per unit length, $k = 2\pi/\lambda$ is the wave vector, λ is the wavelength, $H(z)$ is the Heaviside

step function. The longitudinal electric field within the electron bunch can be written as [27, 28]

$$\mathcal{E}_-(z) = 2\kappa_{\parallel} \int_0^z \cos[k(z-z')]q(z')dz', \quad z \leq L, \quad (2)$$

which is a Volterra equation of the first kind for the function $q(z)$ with the trigonometric kernel $\cos[k(z'-z)]$. If we assume that $\mathcal{E}_-(0) = 0$ at the bunch head, then the solution of Eq. (2) is given by [29],

$$q(z) = \frac{1}{2\kappa_{\parallel}} \left[\mathcal{E}'_-(z) + k^2 \int_0^z \mathcal{E}_-(x) dx \right], \quad (3)$$

where $\mathcal{E}_-(z)$ is a known function, and its derivative is taken over z . Hence, $q(z)$ is defined.

In order to maintain the stability of the drive bunch in the CWA throughout its deceleration, we require the bunch's relative chirp to be constant while being decelerated by the wakefield $\mathcal{E}_-(z)$, based on studies in [24]. This requirement is achieved by having a small linear variation in energy loss within the bunch, where head particles lose more energies than tail particles such that

$$\chi(s) = \frac{1}{E_0(s)} \frac{\partial E}{\partial z} \propto \mathcal{E}'_-(z) \equiv \text{const}, \quad (4)$$

where $E_0(s)$ is the energy of the reference particle, and s is the distance propagated by the bunch in the CWA. This is accomplished by using the electron bunch producing \mathcal{E}_- with a linear variation in z . Similar to Ref. [9], we solve Eq. (3) considering $q(z)$ to be constant in the range $0 \leq z < \xi$ with $\xi = \frac{1}{k} \arccos(\chi/k)$, in which case the continuities of $\mathcal{E}_-(z)$ and $\mathcal{E}'_-(z)$ are preserved over the entire bunch length

$$q(z) = \begin{cases} q_0, & 0 \leq z < \xi, \\ q_0 \left[1 - k\xi \sin(k\xi) + \frac{k^2}{2}\xi^2 \cos(k\xi) + (k \sin(k\xi) - k^2\xi \cos(k\xi))z + \frac{k^2}{2} \cos(k\xi)z^2 \right], & \xi \leq z \leq L, \end{cases} \quad (5)$$

$$q_0 = \frac{6Q}{6L + k^2 \cos(k\xi)(L - \xi)^3 + 3k \sin(k\xi)(L - \xi)^2}.$$

Setting $\chi = 0$, simplifies $q(z)$ to one used in [9]. Figure 1 shows an example of a modified doorstep distribution with an associated wakefield calculated using $L = \lambda$ and $\chi = -\frac{1}{10\lambda}$. In this example we considered a corrugated waveguide with radius $a=1$ mm and fundamental mode frequency $f = 180$ GHz, as discussed in Ref. [31]. The current profile has sharp features that are challenging to realize. Consequently, the distribution defined by Eq. (5)

is used only as a starting point to construct a practically realizable distribution shown in Fig. 2 with similar final properties listed in Table I.

III. A PRELIMINARY DESIGN OF THE DRIVE BUNCH ACCELERATOR

A. Basic considerations

A block diagram of the drive bunch accelerator is shown in Fig. 3. It utilizes a commonly used con-

¹ It has been shown in [10] that a multi-mode Green's function is less effective in producing a high transformer ratio.

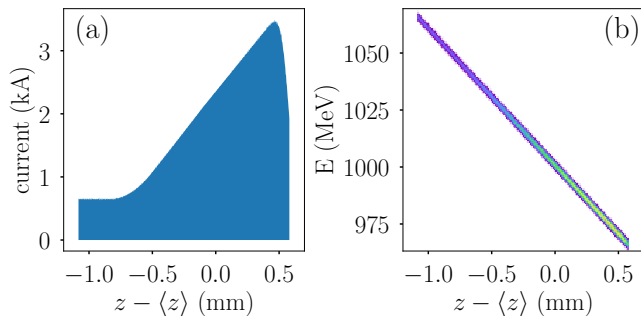


Figure 2. A target drive bunch peak current (a) and longitudinal phase space (b) distributions at the end of the drive bunch accelerator.

Table I. Main parameters associated with the drive bunch distribution shown in Fig. 2.

Bunch parameter	Value	Unit
Charge	10	nC
Reference energy	1	GeV
RMS length	419	μm
Peak current	3.5	kA
RMS fractional energy spread	2.51	%
RMS fractional slice energy spread	0.1	%

figuration (see, for example, [32, 33]) and includes a photocathode-gun-based injector, three linac sections, and two bunch compressors. Linac sections L1 and L2 are based on 650 MHz superconducting (SRF) linac structures, and linac section L39 is based on 3.9 GHz SRF structures. It is used for linearization of the electron distribution in the longitudinal phase space (LPS). Two bunch compressors are labeled as BC1 and BC2. Here we take advantage of the requirement to prepare the drive bunch with the energy chirp seen in Fig. 2(b) and move BC2 to the end of the linac, since we do not need to use the linac to remove the energy chirp after bunch compression.



Figure 3. Block diagram of the drive bunch accelerator.

Using the known LPS distribution $\Phi_f(z_f, E_f)$ at the end of the accelerator, we performed the one-dimensional (1D) backward tracking proposed in [11] to find the LPS distribution $\Phi_i(z_i, E_i)$ at the entrance of L1. We stopped at L1 where the beam energy is approximately 50 MeV considering that 1D tracking may not be reliable at lower energies where transverse and longitudinal space charge effects are stronger. The assumption is that at this point the backward tracking will produce a plausible $\Phi_i(z_i, E_i)$ that can be matched by the injector. Specifically, we constrained the peak current to $I \leq 300$ A and sought $\Phi_i(z_i, E_i)$ with minimal high-order correlations.

A tracking program, TWICE [34], was developed for rapid prototyping of the longitudinal dynamics in the linac without accounting for a transverse motion. The program adopts an approach similar to that used in LiTRACK [35]. An important feature of TWICE is its ability to perform backward tracking including time-reversal of the collective effect, see Appendix A.

The physics model implemented in TWICE includes the geometric wakefields in the accelerating sections, longitudinal space charge effects (LSCs), and coherent synchrotron radiation (CSR). The Green's functions needed for modeling of the geometric wakefield effects in the 650 MHz and 3.9 GHz linac sections were computed using the ECHO software and the empirical formula documented in Ref. [36].

The backward tracking was performed to define $\Phi_i(z_i, E_i)$ using $\Phi_f(z_f, E_f)$, shown in Fig. 2. The following constraints for the accelerator components were observed. First, the BBU-mitigation scheme implemented in the CWA requires a drive bunch with the negative chirp $\frac{\partial E}{\partial z} < 0$, which implies that the longitudinal dispersions of BC1 and BC2 should be $R_{56}^{(1)} > 0$ and $R_{56}^{(2)} > 0$, as we want to maintain a negative chirp throughout the entire accelerator. Second, a total energy gain of ~ 950 MeV in the linac part after the injector is needed. Third, an overall compression factor of ~ 10 is required from two bunch compressors.

In order to enforce all these constraints, TWICE was combined with the multi-objective optimization framework DEAP [37]. The optimization was performed by analyzing the LPS distributions upstream of BC1 and L1 to extract the central energy of the beam slices at every z -coordinate and to fit the slice-energy dependence on z with the polynomial

$$E(z) = c_0 + c_1 z + c_2 z^2 + c_3 z^3, \quad (6)$$

where c_i are constants derived from the fit. The optimizer was requested to minimize the ratio c_2/c_1 in both locations.

B. Discussion of 1D simulation results

A list of optimized accelerator settings found with TWICE backward tracking is given in Table II and the resulting $\Phi_i(z_i, E_i)$ is shown in Fig. 4(a,b). The forward tracking using this distribution recovers $\Phi_f(z_f, E_f)$, as seen in Fig. 4(c,d). The excellent agreement between Fig. 2(a,b) and Fig. 4(c,d) demonstrates the ability of TWICE to properly handle collective effects in both forward and backward tracking.

Each accelerator component serves a special role in obtaining the above-shown result. Linac section L1 provides energy gain and operates far from the crest acceleration to produce the required negative chirp. Linac section L39 corrects a second-order correlation between E and z imprinted on the bunch by the injector and L1

Table II. Optimized parameters from the one-dimensional model.

Parameter	Value	Unit
Accelerating voltage L1	219.46	MV
Phase L1	17.81	deg
Frequency L1	650	MHz
Accelerating voltage L39	9.57	MV
Phase L39	205.72	deg
Frequency L39	3.9	GHz
R_{56} for bunch compressor 1 (BC1)	0.1321	m
T_{566} for bunch compressor 1 (BC1)	-0.1581	m
Accelerating voltage L2	847.69	MV
Phase L2	28	deg
Frequency L2	650	GHz
R_{56} for bunch compressor 2 (BC2)	0.1301	m
T_{566} for bunch compressor 2 (BC2)	0.22	m

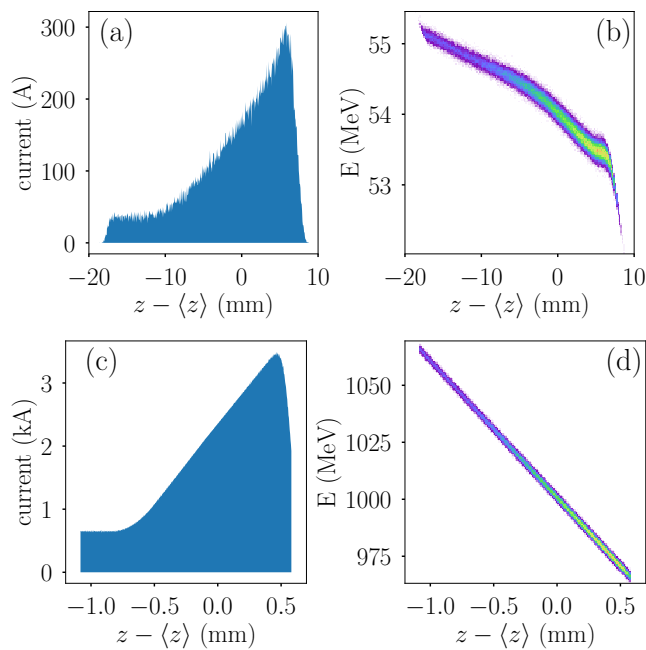


Figure 4. Current (a,c) and LPS (b,d) distributions obtained from the backward-tracking optimization (a,b) and tracked up BC2 end (c,d) to confirm the agreement with the targeted distribution shown in Fig. 2.

before it enters BC1. Linac section L2 operates even further off-crest to impart the necessary large chirp required for maintaining beam stability in the CWA. Both bunch compressors shorten the bunch lengths and impact the LPS distributions. The values of T_{566} selected in both bunch compressors ensure achieving $\Phi_f(z_f, E_f)$ despite the large energy chirp. The use of a negative T_{566} in BC1 and a positive T_{566} in BC2 enables the generation of a doorstep-like initial distribution without giving rise to a current spike, where T_{566} has the effect of shifting the peak of current [38, 39]. In this paper, we adopt the convention that T_{566} with a negative (resp. positive) sign shifts the peak of current distribution to the tail (resp.

head).

The result of the backward-tracking optimization provides only a starting point for obtaining a more realistic solution. For instance, the zigzag feature observed in the tail of the LPS distribution in Fig. 4(b) is challenging to create. In the following sections, we discuss how 1D backward tracking results guide the design of a photocathode-gun-based injector and the downstream accelerator lattice.

IV. INJECTOR DESIGN

Given the required initial LPS distribution obtained from the backward tracking, the next step is to explore whether such LPS distribution is achievable downstream of the injector; our approach relies on temporally shaping the photocathode laser pulse [40].

The injector beamline was modeled using the particle-in-cell beam-dynamics program ASTRA, which includes a quasi-static space-charge algorithm [41]. The program was combined with the DEAP multivariate optimization framework to find a possible injector configuration and the laser pulse shape that realize the desired final bunch distribution while minimizing the transverse-emittance downstream of the photoinjector.

The injector configuration consists of a 200 MHz quarter-wave SRF [42–44], coupled to a 650 MHz accelerator module composed of five 5-cell SRF cavities [45]. The gun includes a high- T_c superconducting solenoid [46] for emittance control.

In the absence of collective effects, the photoemitted electron-bunch distribution mirrors the laser pulse distribution. In practice, image-charge and space-charge effects are substantial during the emission process and distort the electron bunch distribution. Consequently, devising laser-pulse distributions that compensate for the introduced deformities is critical to the generation of bunches with tailored current profiles. The laser pulse distribution is characterized by $I(t, r) = \Lambda(t)R(r)$, where $\Lambda(t)$ and $R(r)$ describe the laser temporal profile and the transverse envelope, respectively. In our simulation, we assumed the transverse distribution to be radially uniform $R(r) = H(r_c - r)$, where $H(r_c - r)$ is Heaviside step function and r_c is the maximum radius. The temporal profile is parameterized as

$$\Lambda(t) = Af(t)S(a(t-f))S(-b(t-g)), \text{ where } \quad (7)$$

$$f(t) = \begin{cases} h, & 0 \leq t < c \\ h + d(t-c)^{d-1}, & c \leq t \leq 1 \\ 0, & \text{elsewhere} \end{cases}$$

where A is the normalization constant; and a, b, c, d, f, g , and h are the parameters controlling the bunch shape. The smooth edges at both ends are characterized by a, b, f, g via the logistic function $S(u) = 1/(1+e^{-u})$; c determines the length of the constant part of the laser pulse analogous to the length of the bunch head of the doorstep

distribution; and h determines the relative amplitude of the constant laser pulse; see Fig. 5. The overall shape

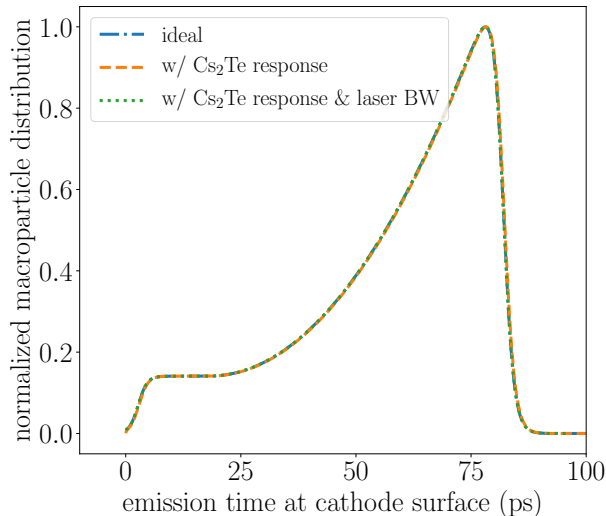


Figure 5. Programmed macroparticle distributions at the photocathode surface: for an optimized laser pulse (blue trace), taking into account the photocathode response (orange trace), and both the cathode response and finite bandwidth (BW) of the laser pulse (green trace). The laser bandwidth is taken to be $\delta f = 2$ THz.

resembles a smoothed version of the door-step distribution. The laser-shape parameters introduced in Eq. (7), the laser spot size, the phase and accelerating voltage of all RF cavities, and the HTS solenoid peak magnetic field were taken as control parameters for the optimization algorithm. The beam kinetic energy was constrained not to exceed 60 MeV. In order to quantify the final distribution, we used the Wasserstein’s distance [47] to quantify how close the shape of the simulated macroparticle distribution at the injector exit $I^{(o)}(z)$ was to the shape of the target macroparticle density distributions $I^{(t)}(z)$ obtained from backward tracking results. Specifically, the Wasserstein’s distance is evaluated as

$$\mathcal{D} = \sum_{i=1} N_b \frac{\|I_i^{(t)} - I_i^{(o)}\|}{N_b}, \quad (8)$$

where $I_i^{(t,o)}$ are the corresponding histograms of the macroparticles’ longitudinal positions over the interval i defined as $[z_i + \delta z, z_i - \delta z]$, with $\delta z \equiv \frac{\max(z) - \min(z)}{N_b}$ being the longitudinal bin size and N_b the number of bins used to compute the histogram. Additionally, we need to have a small beam transverse emittance. Hence, the Wasserstein’s distance and the beam transverse emittance were used as our objective functions to be minimized.

An example of the optimized injector settings is summarized in Table III, and the evolution of the associated

Table III. Optimized parameters for the injector and beam parameters at $s = 11.67$ m from the photocathode surface. The RF-cavity phases are referenced with respect to the maximum-energy phases.

Parameter	Value	Unit
Laser spot radius	2.810	mm
Laser duration	91	ps
RF gun peak electric field	40	MV/m
RF gun phase	1.71	deg
Cavity C1 peak electric field	13.25	MV/m
Cavity C1 phase	11.28	deg
Cavity C2 phase	-15.05	deg
Cavities C2 to C5 peak electric field	20	MV/m
Cavities C3 to C4 phase	0	deg
Cavity C5 phase	20	deg
Cavity C1 distance from the photocathode	2.67	m
Solenoid B-field	0.2068	T
Shape parameter a	93.55	-
Shape parameter b	80.70	-
Shape parameter c	0.196	-
Shape parameter d	3.044	-
Shape parameter f	0.030	-
Shape parameter g	0.900	-
Shape parameter h	0.207	-
Final beam energy	58.7	MeV
Final beam bunch length	7.06	mm
Final beam transverse emittance	8.36	μm
Final beam rms radius	1.64	mm

beam parameters along the beamline are presented in Figs. 6 and 7. The final bunch distributions 11.5 m downstream of the photocathode appears in Fig. 6. The beam transverse phase space indicates some halo population. Ultimately, an alternative laser-shaping approach implementing a spatiotemporal-tailoring scheme could provide better control over the transverse emittance while producing the required shaped electron beams [40]. We also find, as depicted in Fig. 6, that the current distribution tends to have a peak current lower than that desired from the backward tracking result shown in Fig. 4. Although higher currents are possible, they come at the expense of transverse emittance. Consequently, the distribution generated from the injector was considered as an input to the one-dimensional forward tracking simulations. Iterations of one-dimensional forward tracking simulation studies were done to further cross-check accelerator parameters needed for the beam-shaping process. We especially found that the desired final bunch shape at 1 GeV can be recovered by altering the L39 phase and amplitude. Furthermore, the small slice rms energy spread $\sigma_E < 10$ keV simulated from the injector [see Fig. 4(b)] renders the bunch prone to microbunching instability. Consequently, a laser heater is required to increase the uncorrelated energy spread.

The correspondingly revised diagram of the accelerator beamline shown in Fig. 8 was used as a starting point to investigate the performance of the proposed bunch-shaping process with ELEGANT tracking simulations taking into account the transverse beam dynamics.

Another challenge associated with the bunch formation pertains to the temporal resolution of the bunch shaping process. Ultimately, the laser pulse shape can only be controlled on a time scale $\delta t \geq 1/(2\pi\delta f_L)$ limited by the bandwidth of the photocathode laser δf_L . Contemporary laser systems are capable to $\delta t \leq 150$ fs (RMS) [48]. Additionally, the electron bunch shape is also affected by the time response of the photoemission process. Given the required charge of ~ 10 nC, we consider a Cs₂Te photocathode with temporal response numerically investigated in Ref. [49, 50]. Recent measurements confirm that Cs₂Te has a photoemission response time below 370 fs [51]. Figure 5 compares the optimized ideal laser pulse shape described by Eq. (7) with the cases when the photocathode response time and the laser finite bandwidth are taken into account. The added effects have an insignificant impact on the final distribution due to relatively slow temporal variations in the required peak current distribution.

V. FINAL ACCELERATOR DESIGN

The strawman accelerator design developed with the help of 1D simulations provides guidance for the final design of the accelerator.

A. Accelerator components

a. Linacs: For the 650 MHz L1 and L2 SRF linacs we adopted cryomodules proposed for the PIP-II

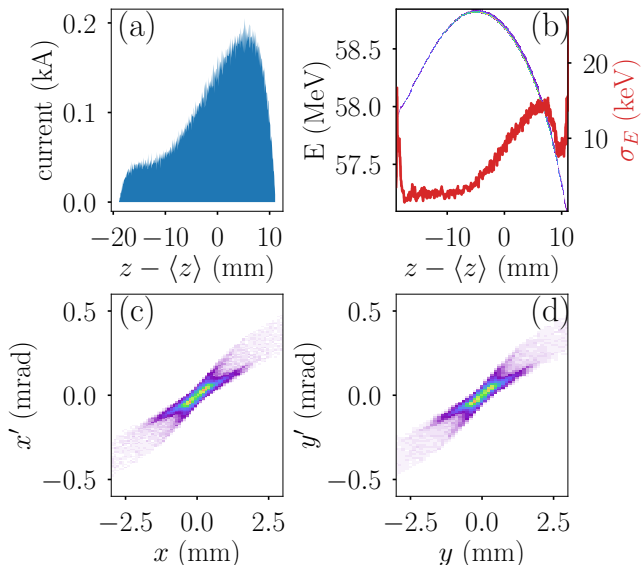


Figure 6. Current profile (a) with associated LPS (b), and horizontal (c) and vertical (d) phase-space distributions simulated with ASTRA at the end of the photoinjector (11.67 m from the photocathode). In plot (b), the red trace represents the slice RMS energy spread σ_E .

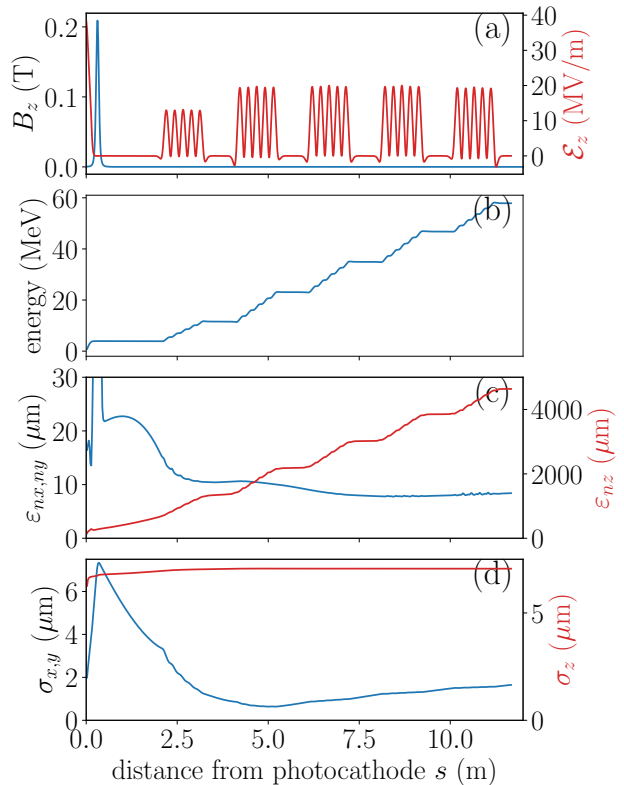


Figure 7. Axial electric \mathcal{E}_z (red trace) and magnetic B_z (blue trace) fields experienced by the reference particle as it propagates along the optimized photoinjector (a) with corresponding kinetic energy (b), transverse (blue) and longitudinal (red) beam emittances (c), and sizes (d) evolving along the injector.



Figure 8. Updated accelerator design, with the addition of the injector beamline and a laser heater section.

project [52]. The linac L1 consists of two cryomodules, and L2 has eight cryomodules. Each cryomodule includes six cavities containing five cells. We assume that in CW operation each cavity provides up to 20 MV/m average accelerating gradients. The quadrupole magnet doublets are located between cryomodules and produce a pseudo-periodic oscillation of the betatron functions. The two cavities used in the 3.9 GHz L39 SRF linac are similar to the cavity described in Ref. [36].

b. Bunch compressors: We use an arc-shaped bunch compressor consisting of a series of FODO cells, where each cell contains two quadrupoles and two dipole magnets. The latter configuration nominally provides a positive R_{56} [53–56]

$$R_{56} \simeq \frac{\theta_{\text{total}}^2 L_{\text{total}}}{4N_{\text{cell}}^2 \sin^2(\psi_x/2)}, \quad (9)$$

where θ_{total} is the total bending angle, L_{total} is the total path length, N_{cell} is the total number of FODO cells, and ψ_x is the horizontal phase advance per cell. The dipole magnet bending angles can be used to tune the R_{56} . The bending angle or dipole polarity from cell to cell does not need to be identical, but the number of cells should be selected to realize a phase advance $\psi_{x,\text{total}} = 2n\pi$ (with n integer) over the compressor to achieve the first-order achromat.

The second-order longitudinal dispersion produced by the bunch compressor is given by [57, 58]

$$T_{566} = \int_0^L \left[\frac{\eta_{1,x}(s')}{\rho(s')} + \frac{\eta_x'^2(s')}{2} \right] ds', \quad (10)$$

where L is the length of the beamline, ρ is the bending radius, $\eta_{1,x}(s) \equiv (E_0^2/2)\partial^2 x(s)/\partial E^2$ is the second-order horizontal dispersion function, and $\eta_x'(s)$ is the derivative of the dispersion function. We incorporate 12 sextupole magnets to control the T_{566} and 12 octupole magnets to cancel the third-order longitudinal transfer-map element U_{5666} computed over BC1. If needed, a non-vanishing value of U_{5666} can enable higher-order control over the LPS correlation [38].

The sextupole and octupole magnets are also used to zero the chromatic transfer-map elements T_{166} , T_{266} , and U_{1666} , resulting in the bunch compressors being achromatic up to the third order.

Figure 9 displays the BC1 configuration along with the evolution of the betatron functions and relevant horizontal chromatic (η_x , $\eta_{1,x}$, and $\eta_{2,x}$) and longitudinal accumulated transfer-map elements ($R_{56}^{0 \rightarrow s}$, $T_{566}^{0 \rightarrow s}$, and $U_{5666}^{0 \rightarrow s}$) up to third order as a function of the beamline coordinate s . It has two arcs, one bending the beam trajectory by 22.92° and another one bending it back. Each bending magnet has the bending angle $\theta = 2.865^\circ$. This design eases the requirement on the sextupole-magnet strength required to provide a $T_{566} < 0$; see Table II. The strengths of the sextupole magnets were optimized using ELEGANT to achieve the required T_{566} across BC1 while obtaining a second-order achromat by constraining $T_{166} = T_{266} = 0$. The three pairs of sextupole magnets in the second arc are mirror-symmetric to the first three pairs, with opposite-polarity magnet strengths. During the design process, the first pair of sextupole magnets was inserted close to the region of the first arc with the highest dispersion for tuning the desired T_{566} ; its mirror symmetry pair was placed in the second arc and separated by 2π phase advance. Another two pairs of sextupole magnets were subsequently inserted for tuning T_{166} . Similarly, their mirror symmetry pairs were separated by 2π phase advance. Finally, six pairs of octupole magnets were inserted to zero the overall U_{i666} $i = 1, 2, 5$ transfer-map elements, where the same design process was employed. The BC2 compressor requires both R_{56} and T_{566} to be positive, which is naturally provided by the arc bunch compressor introduced earlier. It has a total bending angle of 32.63° , and each dipole has a bending angle of 4.079° . Similar to BC1, we used sextupole- and

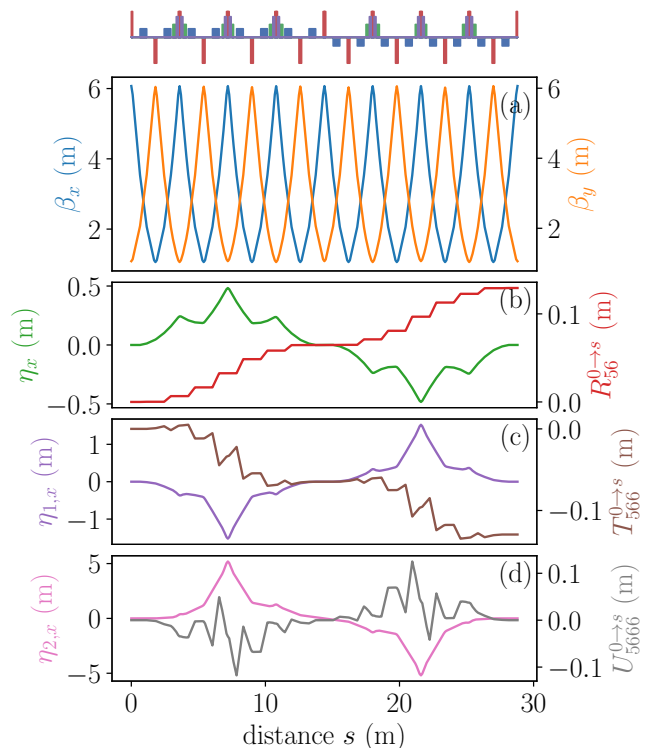


Figure 9. Layout of bunch compressor BC1 (top diagram) with evolution of associated betatron function (a) and pertinent linear (b), second-order (c), and third-order (d) transfer-map elements along the beamline (with $s = 0$ corresponding to the beginning of BC1). In plots (b-d) the left and right axes refer to the horizontal chromatic functions $\eta_{i,x}$ and accumulated longitudinal transfer-map elements from 0 to location s along BC1. In the top diagram the red, blue, green, and purple rectangles correspond, respectively, to quadrupole, dipole, sextupole, and octupole magnets.

octupole-magnet families to adjust both T_{566} and U_{5666} and produce the third-order achromat. The BC2 lattice appears in Fig. 10 along with the evolution of the betatron functions and relevant chromatic elements. Finally, the layout of the two bunch compressors is presented in Fig. 11.

c. Matching sections: All accelerator components are connected using matching sections composed of quadrupole magnets and drift spaces.

The evolution of the betatron functions from the injector exit up to the end of BC2 appears in Fig. 12. Throughout the entire accelerator, the betatron functions are maintained to values $\beta_{x,y} < 30$ m.

B. Tracking and optimization

The beam distribution obtained at the exit of the injector was used as input to ELEGANT for tracking and optimization. We found that we need to increase the slice energy spread to ~ 75 keV using the laser heater

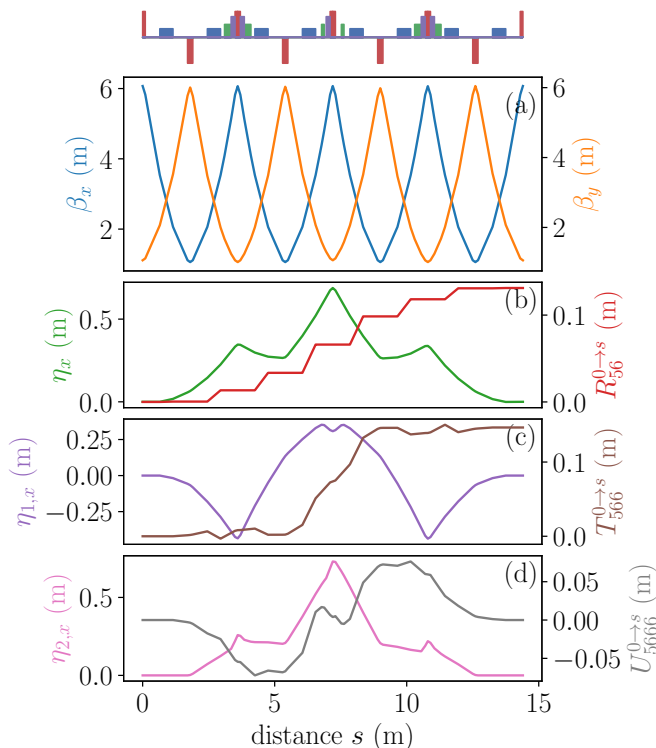


Figure 10. Layout of bunch compressor BC2 (top diagram) with evolution of associated betatron function (a) and pertinent linear (b), second-order (c), and third-order (d) transfer-map elements along the beamline (with $s = 0$ corresponding to the beginning of BC2). In plots (b-d) the left and right axes refer to the horizontal chromatic functions $\eta_{i,x}$ and accumulated longitudinal transfer-map elements from 0 to location s along BC2. The top diagram follows the same conventions as in Fig. 9.

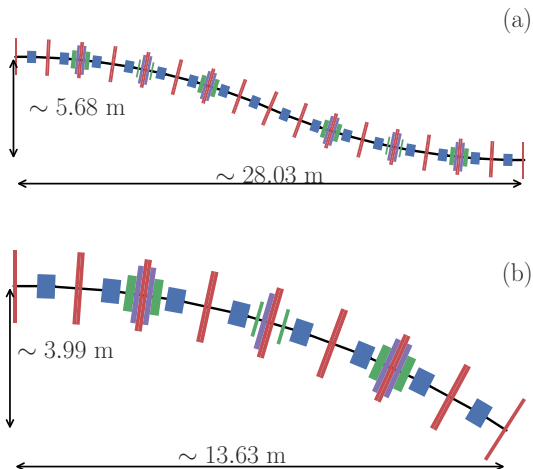


Figure 11. The geometry of the bunch compressors BC1 (a) and BC2 (b), where red, blue, green, and purple rectangles are quadrupoles, dipoles, sextupoles, and octupoles magnets, respectively.

to suppress the microbunching instability [59, 60]. However, in this study, we numerically added random noise with Gaussian distribution to the macroparticles' energy using the SCATTER element available in ELEGANT. Thus, Fig. 13 shows the actual LPS distribution used at the beginning of the accelerator in tracking studies.

The accelerator settings obtained with TWICE were used as a starting point in the accelerator optimization including transverse effects. The fine-tuning of the above-described accelerator components was accomplished using ELEGANT. A multi-objective optimization was applied to determine the twelve accelerator parameters controlling the longitudinal dynamics, i.e., voltages and phases of L1, L2, L39, and values of R_{56} , T_{566} in two bunch compressors. The resulting beam distribution obtained downstream of BC2 was then used to compute the wakefield generated in a 180 GHz corrugated waveguide considered for the role of the wakefield accelerator in [31]. The resulting peak accelerating field and transformer ratio were then adopted as objective functions to be maximized with the accelerator parameters as control variables. The trade-off between peak accelerating field and transformer ratio was quantified in Eq. (30) of Ref. [10], hence providing a good measure to verify whether our optimization reaches the optimal Pareto front. The op-

Table IV. Main accelerator parameters and beam parameters at the end of BC2.

Parameter	Value	Unit
Accelerating voltage L1	193.22	MV
Phase L1	21.64	deg
Frequency L1	650	MHz
Accelerating voltage L39	9.73	MV
Phase L39	202.52	deg
Frequency L39	3.9	GHz
R_{56} for bunch compressor 1 (BC1)	0.1294	m
T_{566} for bunch compressor 1 (BC1)	-0.1294	m
U_{5666} for bunch compressor 1 (BC1)	0	m
Accelerating voltage L2	857.92	MV
Phase L2	26.05	deg
Frequency L2	650	MHz
R_{56} for bunch compressor 2 (BC2)	0.1312	m
T_{566} for bunch compressor 2 (BC2)	0.1465	m
U_{5666} for bunch compressor 2 (BC1)	0	m
Final beam energy	998	MeV
Final beam bunch length	414	μm
Final beam normalized emittance, ε_{nx}	31	μm
Final beam normalized emittance, ε_{ny}	12	μm
Peak accelerating wakefield $ \mathcal{E}_+ $	94.3	MV/m
Peak decelerating wakefield $ \mathcal{E}_- $	18.8	MV/m
Transformer ratio \mathcal{R}	5.0	-

timal accelerator settings and final beam parameters are summarized in Table IV. The LPS distribution at the end of the accelerator is shown in Fig. 14. We also calculated that the ~ 1 GeV, 10 nC electron bunch having this distribution produces a peak wakefield of 94.26 MV/m with a transformer ratio of 5 propagating in a corrugated waveguide. Figure 15 demonstrates that our optimiza-

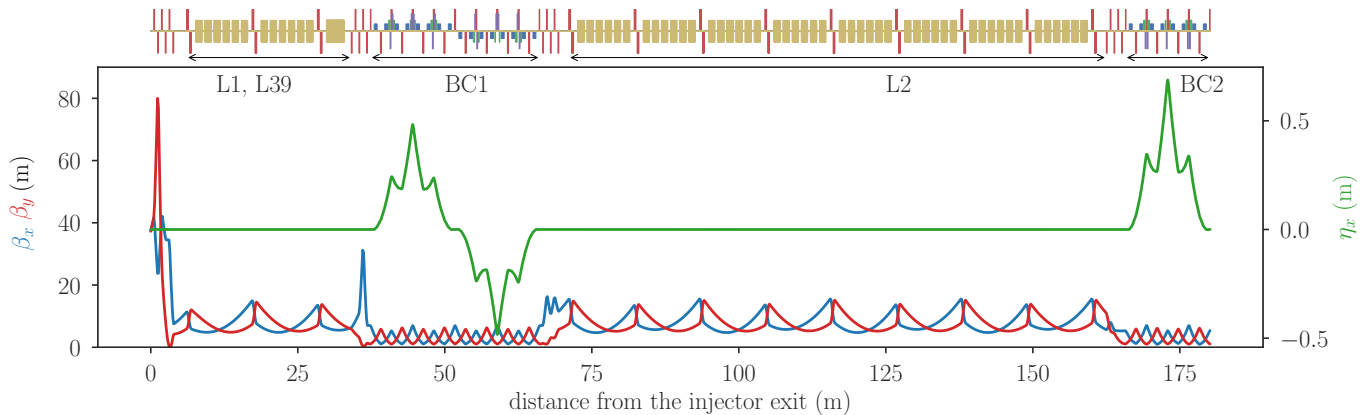


Figure 12. Evolution of the betatron (left axis) and horizontal dispersion (right axis) functions along the proposed linac. The vertical dispersion is zero throughout the linac. The magnetic-lattice color coding for the element follows Fig. 9 with the accelerating cavities shown as gold rectangles.

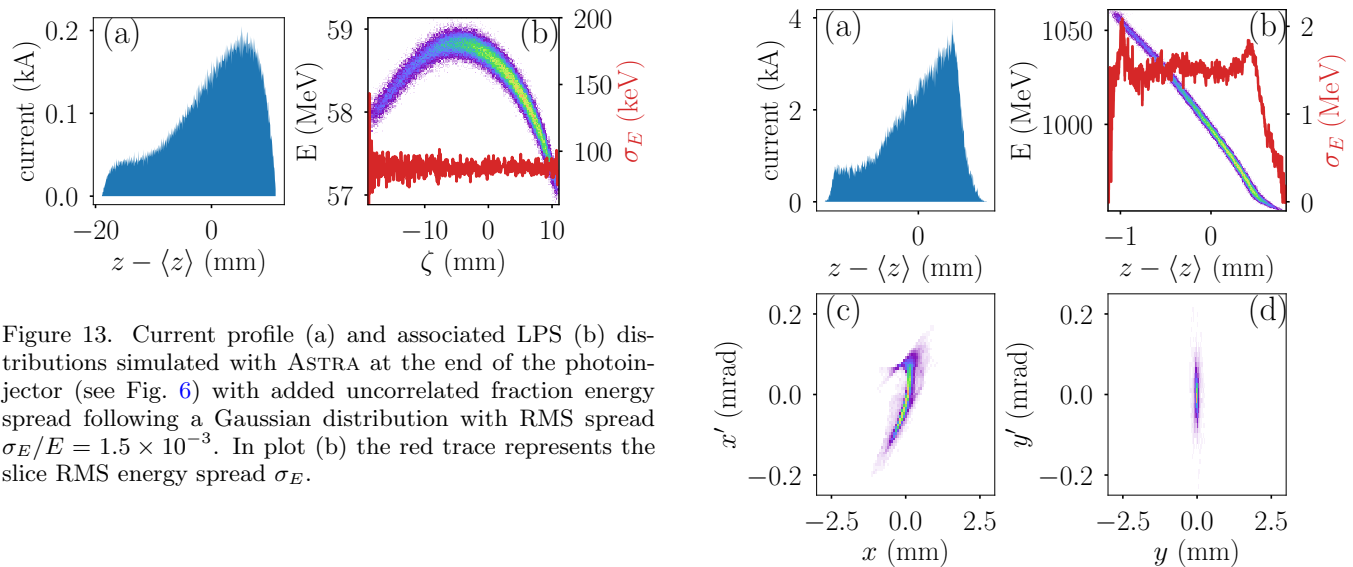


Figure 13. Current profile (a) and associated LPS (b) distributions simulated with ASTRA at the end of the photoinjector (see Fig. 6) with added uncorrelated fraction energy spread following a Gaussian distribution with RMS spread $\sigma_E/E = 1.5 \times 10^{-3}$. In plot (b) the red trace represents the slice RMS energy spread σ_E .

tion has reached the optimal set of solutions, where the Pareto front closely follows the analytically calculated tradeoff curve [10]. The obtained current profile produces a wakefield amplitude $\sim 15\%$ lower than the one expected from the ideal distribution for a transformer ratio $\mathcal{R} \simeq 5$. Such an agreement gives confidence in our optimization approach based on the trade-off between peak accelerating field and transformer ratio. The simulations also indicate that the horizontal transverse emittance increases to $\varepsilon_{nx} = 31 \mu\text{m}$ due to the CSR and chromatic aberrations in the electron bunch having large correlated energy variations. Although significant, this emittance dilution is still acceptable.

Our main result is shown in Fig. 16. It compares the final distribution and wakefield with that of the target distribution and wakefield from Fig. 2. A good agreement manifests that, indeed, the drive electron bunch with a highly asymmetric peak current profile can be obtained without employing the collimators.

A comparison of Tables III and IV indicates that the

Figure 14. Current (a) with associated LPS (b), and transverse horizontal (c) and vertical (d) phase-space distributions simulated with ELEGANT at the end of BC2 using the optimized linac and bunch-compressor settings summarized in Table IV and the injector distributions from Fig. 13. In plot (b) the red trace represents the slice RMS energy spread σ_E .

final accelerator settings optimized by ELEGANT deviate less than 10% from those obtained with TWICE. It justifies the strategy taken in this study to solve the difficult problem of formation of temporally shaped electron bunches for a beam-driven collinear wakefield accelerator in two steps.

The nonlinear correlation observed in the tail of the LPS distribution downstream of BC2 [see Fig. 14(b, blue trace)] originates from the CSR. As the beam is compressed inside the bunch compressors, its tail experiences a stronger CSR force due to its peak current being higher

than the rest of the bunch. It is worth noting that ELEGANT uses a 1D projected model to treat the CSR effect. The applicability of such a 1D treatment is conditioned by the Derbenev's criterion [61], which suggests that projecting the bunch distribution onto a line-charge distribution may overestimate the CSR force, particularly when the bunch has a large transverse-to-longitudinal aspect ratio $\mathcal{A}(s) \equiv (\sigma_x(s)/\sigma_z(s)) \sqrt{(\sigma_x(s)/\rho(s))}$. In our design, the condition $\mathcal{A} \ll 1$ was not rigorously followed (but rather the softer condition $\mathcal{A} < 1$ was achieved), suggesting that the impact of CSR may be overestimated in some regions of the bunch compressors.

We also note that the final beam distribution exhibits significant longitudinal-horizontal ($z-x$) correlations due to CSR effects; see Fig. 17. Although the associated projected-emittance dilution is tolerable, the electrons in the longitudinal slices with the horizontal offsets seen in Fig. 17(c) will excite transverse wakefields in the CWA and ultimately seed the BBU instability. These offsets come from CSR-induced energy loss occurring in the BC2

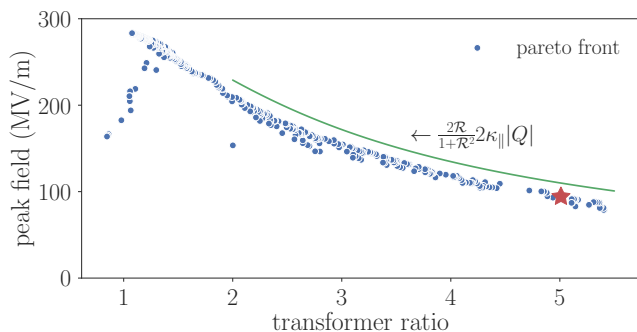


Figure 15. Comparison of the Pareto front with the analytical trade-off curve between the peak field and transformer ratio described by Eq. (30) of Ref. [10]. Each blue dot represents a numerically simulated configuration with the red star representing the configuration with parameters listed in Table IV.

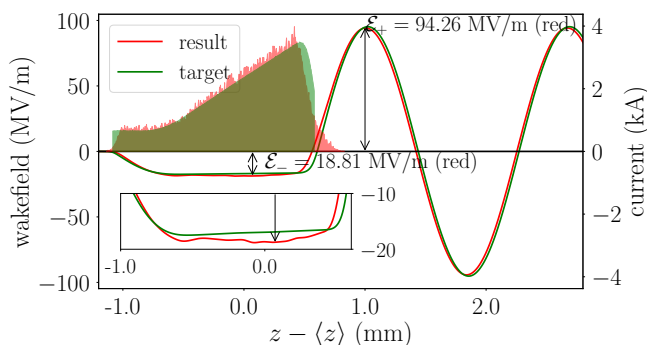


Figure 16. Target (from Fig. 2) and optimized final current distributions (respectively shown as green- and red-shaded curves) with associated wakefields (respectively displayed as green and red traces). The transformer ratio for the simulated distribution is $\mathcal{R} = 5.0$.

that breaks the achromatic property of this beamline. Understanding the impact of this distribution feature in the CWA linac along with finding mitigation techniques is a current research focus.

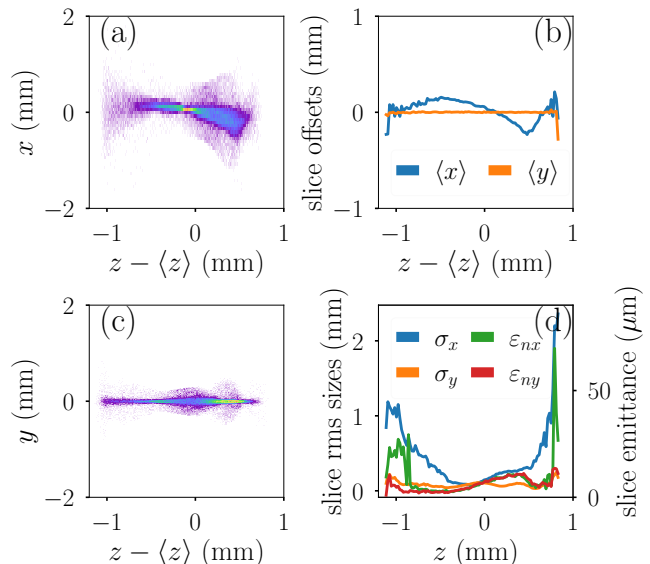


Figure 17. Final (z, x) (a) and (z, y) (c) beam distributions corresponding to the data shown in Fig. 14, and slice analysis for positions $\langle x \rangle$ and $\langle y \rangle$ (b) and RMS beam size and emittances (d).

C. Impact of errors

In order to validate the robustness of the proposed design, it is instructive to investigate the sensitivity of the proposed shaping technique to shot-to-shot jitters of the amplitude and phase of the accelerating field in the linac's structures. Consistent with LCLS-II specifications [62], we considered the relative RMS amplitude jitter of 0.01% and the phase jitter of 0.01 degree. For simplicity, we assume that the injector produced identical bunches, as shown in Fig. 6, and performed 100 simulations of the accelerator beamline (from the injector exit to the exit of BC2) for different random realizations of the phase and amplitude for linacs L1, L2, and L39. The errors in linac settings were randomly generated using Gaussian probability function with standard deviations of 0.01% and 0.01°. Figure 18 presents the wakefield averaged over the 100 simulations and indicates that a stable transformer ratio 5.00 ± 0.05 can be maintained owing to the stable beam produced in the superconducting linac.

Likewise, we observe the impact of charge fluctuation on the shaping to be tolerable. Cathode-to-end simulations combining ASTRA and ELEGANT indicate that a relative charge variation of +2% (resp. -2%) yields a relative change in the transformer ratio of -2% (resp. +1%) and

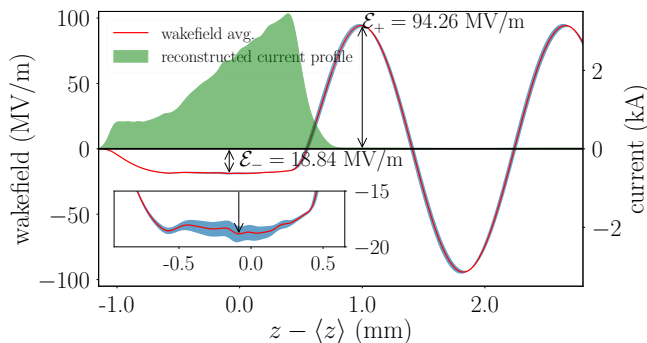


Figure 18. Wakefields obtained from 100 simulations with jitter in linacs L1, L2, and L39. All cavities are taken to have relative jitter in accelerating voltage of 0.01% and phase jitter 0.01°. The red line shows the average wakefield while the blue shaded region represents the fluctuation of wakefields due to jitter over 100 random realizations of the linac settings. The average transformer ratio is 5.00 ± 0.05 . The reconstructed current profile (green-shaded curve) is obtained numerically using Eq. (3).

a relative variation in peak field of -1.7% (resp. +1.7%); see Fig. 19.

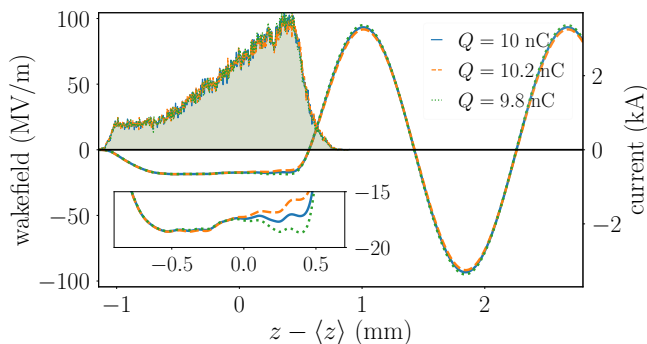


Figure 19. Current distribution (shaded curves, left axis) and associated wakefields (traces) for the nominal charge and $\pm 2\%$ relative change in charge (9.8 and 10.2 nC).

VI. SUMMARY

We have presented the design of an accelerator capable of generating 1 GeV electron bunches with a highly asymmetric peak current profile and a large energy chirp required for a collinear wakefield accelerator. It has been achieved without the use of collimators. Our approach is based on *ab-initio* temporal shaping of the photocathode laser pulse followed by nonlinear manipulations of the electron distribution in the longitudinal phase space throughout the accelerator using collective effects and precision control of the longitudinal dispersion in two bunch compressors up to the third order. Finding the optimal design consisted of first implementing a simpli-

fied accelerator model and using it for backward tracking of the longitudinal phase space distribution of electrons through the main accelerator to provide the longitudinal phase space distribution required from the injector. The program TWICE was developed to support such a capability and used to optimize the global linac parameters and time-of-flight properties of bunch compressors. Second, the simulation of the photo-injector using ASTRA was performed to generate the required distribution. Third, the linac design was refined using ELEGANT to account for the transverse beam dynamics. Finally, formation of longitudinally shaped drive bunches capable of producing in the collinear wakefield accelerator a transformer ratio of ~ 5 and a peak accelerating wakefield close to 100 MV/m has been numerically demonstrated.

Although the proposed accelerator design is promising, we note that further work is required to investigate whether the same accelerator can accelerate the low-charge, low-emittance “witness bunches” that would be accelerated to multi-GeV energies in the collinear wakefield accelerator and used for the generation of x-rays in the downstream free-electron laser. Discussion of this research is the subject of a forthcoming publication.

ACKNOWLEDGMENTS

The authors are grateful to Dr. Stanislav Baturin (NIU) for useful discussions. WHT thanks Y. Park (UCLA) for several discussions on simulation studies. This work is supported by the U.S. Department of Energy, Office of Science, under award No. DE-SC0018656 with Northern Illinois University and contract No. DE-AC02-06CH11357 with Argonne National Laboratory.

Appendix A: One-dimensional tracking model

A simple one-dimensional tracking program TWICE [34] was developed for rapid assessment of the longitudinal dynamics of electrons in linear accelerators. The program adopts an approach similar to the one used in LiTRACK [35], where only the accelerator components affecting the longitudinal beam dynamics are considered and modeled analytically. A detailed description of TWICE is published in [34]. In brief, the beam is represented by a set of N macroparticles with identical charges Q/N and given a set of initial LPS coordinates (z_i, E_i) . A transformation $(z_f, E_f) = f(z_i, E_i)$ is applied to obtain final coordinates in the LPS.

a. Single particle dynamics

In TWICE the transformation for a macroparticle with coordinates (z_i, E_i) passing through a radiofrequency

(RF) linac is given by

$$\begin{pmatrix} z_f \\ E_f \end{pmatrix} = \begin{pmatrix} z_i \\ E_i(z_i) \pm eV \cos(kz_i + \varphi) \end{pmatrix}, \quad (\text{A1})$$

where V , k , and φ are, respectively, the accelerating voltage, wave-vector amplitude, and off-crest phase associated with the accelerating section, and e is the electronic charge. In the latter and following equations the \pm sign indicates the forward (+) and backward (-) tracking process detailed in Sec. A 0 c. Similarly, the transformation through a longitudinally dispersive section, such as a bunch compressor, is given by

$$\begin{pmatrix} z_f \\ E_f \end{pmatrix} = \begin{pmatrix} z_i \pm \left[R_{56} \frac{E_i - E_0}{E_0} + T_{566} \left(\frac{E_i - E_0}{E_0} \right)^2 \right] \\ E_i \end{pmatrix}, \quad (\text{A2})$$

where E_0 is the reference-particle energy assumed to remain constant during the transformation, and $R_{56} \equiv E_0 \frac{\partial z_f}{\partial E_i}$ and $T_{566} \equiv \frac{E_0^2}{2} \frac{\partial^2 z_f}{\partial E_i^2}$ are the first- and second-order longitudinal-dispersion functions introduced by the beamline. It should be noted that, given our LPS coordinate conventions, a conventional four-bend ‘‘chicane’’ magnetic bunch compressor has a longitudinal dispersion $R_{56} > 0$. The latter equation ignores energy loss, e.g., due to incoherent synchrotron radiation, occurring in the beamline magnets.

b. Collective effects

In TWICE, we implemented collective effects as an energy kick approximation using the transformation

$$\begin{pmatrix} z_f \\ E_f \end{pmatrix} = \begin{pmatrix} z_i \\ E_i(z_i) \pm \Delta E(z_i) \end{pmatrix}, \quad (\text{A3})$$

where $\Delta E(z)$ represents the energy change associated with the considered collective effect. The treatment of collective effects is modeled as a z -dependent energy kick $\Delta E(z)$ taken downstream of beamline elements as specified for the forward and backward tracking with the diagram shown in Fig. 20. The implemented collective effects include wakefields modeled after a user-supplied Green’s function, one-dimensional steady-state coherent synchrotron radiation (CSR), and longitudinal space charge (LSC) described via an impedance. The collective effects require the estimation of the beam’s charge density, which is done in TWICE either using a standard histogram binning method with noise filtering or via the kernel-density estimation technique [63].

In order to model the impact of a wakefield, the charge distribution $q(z)$ is directly used to compute the wake potential given a tabulated Green’s function

$$W(z) = \int_0^z q(z') G(z - z') dz'. \quad (\text{A4})$$

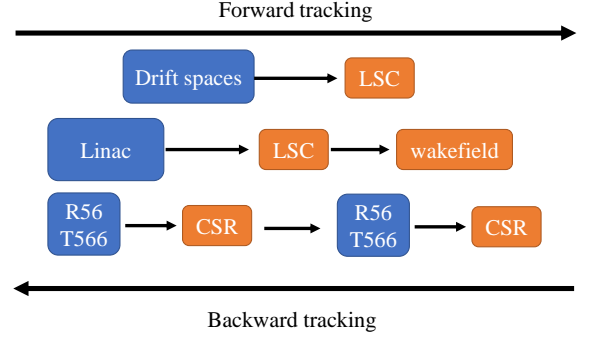


Figure 20. Treatment of collective effects as energy kicks downstream of beamline elements. In forward (resp. backward) tracking, transformations of beamline elements (resp. energy kicks) were applied, followed by energy kicks (resp. beamline elements).

The change in energy is computed as $\Delta E(z) = LW(z)$, where L is the effective length where the beam experiences the wakefield.

The LSC is implemented using a one-dimensional model detailed in [64], where the impedance per unit length is

$$Z(k) = i \frac{Z_0}{\pi \gamma r_b} \frac{1 - 2I_1(\xi_b)K_1(\xi_b)}{\xi_b}, \quad (\text{A5})$$

where $\xi_b \equiv kr_b/\gamma$; I_1 and K_1 are modified Bessel functions of the first and second kind, respectively; and k , Z_0 and r_b are, respectively, the wave-vector amplitude, impedance of free space and a user-defined transverse beam radius, and γ is the Lorentz factor. Given the charge density, the Fourier-transformed current density $\tilde{I}(k)$ is derived from

$$\tilde{I}(k) = \mathcal{F}[cq(z)], \quad (\text{A6})$$

with \mathcal{F} representing the Fourier transform. The change in energy is computed as

$$\Delta E = -\mathcal{F}^{-1}[eZ(k)\tilde{I}(k)L], \quad (\text{A7})$$

where \mathcal{F}^{-1} is the inverse Fourier transform, and L is the effective distance along which the LSC interaction occurs. In order to account for LSC during acceleration, γ is replaced by the geometry average $\sqrt{\gamma_i \gamma_f}$ of the Lorentz factors computed at the entrance γ_i and exit γ_f of the linac section.

Finally, CSR energy kicks are applied downstream of the dispersive beamline elements. For instance, a CSR energy kick can be applied after a dispersive element with user-defined length and angle described by R_{56} and T_{566} . The effect of CSR is described using a one-dimensional model commonly implemented in other beam-dynamics program [65]. To simplify the calculation, only the

steady-state CSR is considered in TWICE. The energy loss associated with CSR is obtained from [66]²,

$$\Delta E(z) = \rho\theta \frac{dE}{dct} = -\theta \frac{\gamma m_e c^2 r_e}{e} \int_{-\infty}^z \frac{\partial q(z')}{\partial z'} I_{csr}(z, z') dz', \quad (\text{A8})$$

with the integral kernel defined as

$$I_{csr}(z, z') = \frac{4u(u^2 + 8)}{(u^2 + 4)(u^2 + 12)}, \quad (\text{A9})$$

where θ is the angle, $m_e c^2$ is the electron rest mass energy, r_e is the classical electron radius and the variable u is the solution of $\frac{\gamma^3(z-z')}{\rho} = \frac{u^3}{24} + \frac{u}{2}$. CSR introduces an energy loss strongly dependent on the bunch length, which varies within the dispersive sections used to compress the bunch. Consequently, the longitudinally dispersive beamlines are segmented into several elements with individual (R_{56}, T_{566}) parameters. A CSR kick is ap-

plied after each of the elements. A conventional chicane-type bunch compressor is usually broken into two sections (two mirror-symmetric doglegs) but can in principle be divided into an arbitrary number of segments to improve the resolution at the expense of computational time.

c. Backward tracking

An important feature of TWICE is its capability to track the beam in the forward or backward directions (indicated by the \pm sign in Eqs. (A2) and (A3)) in the presence of collective effects [so far LSC, CSR, and wakefield effects are included]. The effects of LSC and wakefield are straightforward to implement as they only involve a change in energy, while handling of the CSR requires extra care since the particles' positions also change throughout the dispersive section. Therefore, an energy kick is applied after the beamline element in the forward-tracking mode and before the beamline element in backward-tracking mode, as shown in Fig. 20. Although the treatment of CSR is not exact, it nonetheless provides a good starting point to account for the effect.

-
- [1] G. Voss and T. Weiland, *The wake field acceleration mechanism*, Tech. Rep. DESY-82-074 (DESY, 1982).
- [2] R. J. Briggs, T. J. Fessenden, and V. K. Neil, Electron autoacceleration, in *Proceedings, 9th International Conference on the High-Energy Accelerators* (1974) p. 278.
- [3] M. Friedman, Autoacceleration of an intense relativistic electron beam, *Phys. Rev. Lett.* **31**, 1107 (1973).
- [4] E. A. Perevedentsev and A. N. Skrinsky, On the Use of the Intense Beams of Large Proton Accelerators to Excite the Accelerating Structure of a Linear Accelerator, in *Proc. 6th All-Union Conference Charged Particle Accelerators, Dubna (Institute of Nuclear Physics, Novosibirsk, USSR, 1978)*, Vol. 2 (1978) p. 272, English version is available in *Proceedings of the 2nd ICFA Workshop on Possibilities and Limitations of Accelerators and Detectors* (1979) p. 61.
- [5] A. M. Sessler, The free electron laser as a power source for a high-gradient accelerating structure, *AIP Conference Proceedings* **91**, 154 (1982).
- [6] P. Chen, J. M. Dawson, R. W. Huff, and T. Katsouleas, Acceleration of electrons by the interaction of a bunched electron beam with a plasma, *Phys. Rev. Lett.* **54**, 693 (1985).
- [7] Y. Chin, The Wake Field Acceleration Using a Cavity of Elliptical Cross Section, in *12th international linear accelerator conference* (1983) pp. 159–161.
- [8] W. Gai, P. Schoessow, B. Cole, R. Konecny, J. Norem, J. Rosenzweig, and J. Simpson, Experimental demonstration of wake-field effects in dielectric structures, *Phys. Rev. Lett.* **61**, 2756 (1988).
- [9] K. L. Bane, P. Chen, and P. B. Wilson, On collinear wake field acceleration, *Proceedings of the 1985 Particle Accelerator Conference (PAC1985): Accelerator Engineering and Technology Vancouver, BC May 13-16, 1985* **32**, 3524 (1985).
- [10] S. S. Baturin and A. Zholents, Upper limit for the accelerating gradient in the collinear wakefield accelerator as a function of the transformer ratio, *Phys. Rev. Accel. Beams* **20**, 061302 (2017).
- [11] M. Cornacchia, S. Di Mitri, G. Penco, and A. A. Zholents, Formation of electron bunches for harmonic cascade x-ray free electron lasers, *Phys. Rev. ST Accel. Beams* **9**, 120701 (2006).
- [12] G. Penco, M. Danailov, A. Demidovich, E. Allaria, G. De Ninno, S. Di Mitri, W. M. Fawley, E. Ferrari, L. Giannessi, and M. Trovó, Experimental Demonstration of Electron Longitudinal-Phase-Space Linearization by Shaping the Photoinjector Laser Pulse, *Phys. Rev. Lett.* **112**, 044801 (2014).
- [13] F. Lemery and P. Piot, Tailored electron bunches with smooth current profiles for enhanced transformer ratios in beam-driven acceleration, *Phys. Rev. Spec. Top. Accel. Beams* **18**, 081301 (2015).
- [14] B. Jiang, C. Jing, P. Schoessow, J. Power, and W. Gai, Formation of a novel shaped bunch to enhance transformer ratio in collinear wakefield accelerators, *Phys. Rev. ST Accel. Beams* **15**, 011301 (2012).
- [15] G. Ha, M. H. Cho, W. Namkung, J. G. Power, D. S. Doran, E. E. Wisniewski, M. Conde, W. Gai, W. Liu, C. Whiteford, Q. Gao, K.-J. Kim, A. Zholents, Y.-E. Sun, C. Jing, and P. Piot, Precision Control of the Electron Longitudinal Bunch Shape Using an Emittance-Exchange Beam Line, *Phys. Rev. Lett.* **118**, 104801 (2017).

² The variable z here for CSR calculation refers to the relative position from the bunch centroid with bunch head at $z > 0$.

- [16] Q. Gao, G. Ha, C. Jing, S. P. Antipov, J. G. Power, M. Conde, W. Gai, H. Chen, J. Shi, E. E. Wisniewski, D. S. Doran, W. Liu, C. E. Whiteford, A. Zholents, P. Piot, and S. S. Baturin, Observation of High Transformer Ratio of Shaped Bunch Generated by an Emittance-Exchange Beam Line, *Phys. Rev. Lett.* **120**, 114801 (2018).
- [17] P. Piot, C. Behrens, C. Gerth, M. Dohlus, F. Lemery, D. Mihalcea, P. Stoltz, and M. Vogt, Generation and Characterization of Electron Bunches with Ramped Current Profiles in a Dual-Frequency Superconducting Linear Accelerator, *Phys. Rev. Lett.* **108**, 034801 (2012).
- [18] W. K. H. Panofsky and M. Bander, Asymptotic Theory of Beam Break-Up in Linear Accelerators, *Review of Scientific Instruments* **39**, 206 (1968).
- [19] V. K. Neil, L. S. Hall, and R. K. Cooper, Further Theoretical Studies Of The Beam Breakup Instability, Part. Accel. **9**, 213 (1979).
- [20] A. W. Chao, B. Richter, and C.-Y. Yao, Beam emittance growth caused by transverse deflecting fields in a linear accelerator, *Nucl. Instrum. Methods* **178**, 1 (1980).
- [21] V. E. Balakin, A. V. Novokhatsky, and V. P. Smirnov, VLEPP: TRANSVERSE BEAM DYNAMICS, Proceedings, 12th International Conference on High-Energy Accelerators, HEACC 1983: Fermilab, Batavia, August 11-16, 1983 **C830811**, 119 (1983).
- [22] C. Li, W. Gai, C. Jing, J. G. Power, C. X. Tang, and A. Zholents, High gradient limits due to single bunch beam breakup in a collinear dielectric wakefield accelerator, *Phys. Rev. ST Accel. Beams* **17**, 091302 (2014).
- [23] D. Y. Shchegolkov, E. I. Simakov, and A. A. Zholents, Towards a Practical Multi-Meter Long Dielectric Wakefield Accelerator: Problems and Solutions, *IEEE Transactions on Nuclear Science* **63**, 804 (2016).
- [24] S. S. Baturin and A. Zholents, Stability condition for the drive bunch in a collinear wakefield accelerator, *Phys. Rev. Accel. Beams* **21**, 031301 (2018).
- [25] A. Zholents *et al.*, A Conceptual Design of a Compact Wakefield Accelerator for a High Repetition Rate Multi User X-ray Free-Electron Laser Facility, in *Proc. 9th International Particle Accelerator Conference (IPAC'18), Vancouver, BC, Canada, April 29-May 4, 2018*, International Particle Accelerator Conference No. 9 (JACoW Publishing, Geneva, Switzerland, 2018) pp. 1266–1268, <https://doi.org/10.18429/JACoW-IPAC2018-TUPMF010>.
- [26] G. J. Waldschmidt and others, Design and Test Plan for a Prototype Corrugated Waveguide, in *Proc. 9th International Particle Accelerator Conference (IPAC'18), Vancouver, BC, Canada, April 29-May 4, 2018*, International Particle Accelerator Conference (JACoW Publishing, Geneva, Switzerland, 2018) pp. 1550–1552.
- [27] B. Zotter and S. Kheifets, *Impedances and Wakes in High Energy Particle Accelerators* (World Scientific Publishing Company, 1998).
- [28] A. Chao, *Physics of Collective Beam Instabilities in High Energy Accelerators* (Wiley and Sons, New York, 1993).
- [29] A. Polyanin and A. Manzhairov, *Handbook of Integral Equations* (CRC Press, Boca Raton, 1998).
- [30] I. Zagorodnov, K. L. F. Bane, and G. Stupakov, Calculation of wakefields in 2D rectangular structures, *Phys. Rev. ST Accel. Beams* **18**, 104401 (2015).
- [31] A. E. Siy, G. J. Waldschmidt, and A. Zholents, Design of a compact wakefield accelerator based on a corrugated waveguide, in *Proc. 2019 North American Particle Accelerator Conference (NAPAC2019), Lansing, MI, USA, September 1-6, 2019* (JACoW, Geneva, Switzerland, 2019) pp. 232–235.
- [32] J. Arthur and others, *Linac Coherent Light Source (LCLS) conceptual design report*, SLAC Report SLAC-R-593 (Stanford Linear Accelerator Center, 2002).
- [33] R. A. Bosch, K. J. Kleman, and J. Wu, Modeling two-stage bunch compression with wakefields: Macroscopic properties and microbunching instability, *Phys. Rev. ST Accel. Beams* **11**, 090702 (2008).
- [34] W. Tan, P. Piot, and A. Zholents, Longitudinal Beam-Shaping Simulation for Enhanced Transformer Ratio in Beam-Driven Accelerators, in *2018 IEEE Advanced Accelerator Concepts Workshop (AAC)* (2018) pp. 190–194.
- [35] K. L. F. Bane and P. Emma, Litrack: A Fast Longitudinal Phase Space Tracking Code with Graphical User Interface, in *Proceedings of the 2005 Particle Accelerator Conference* (2005) pp. 4266–4268.
- [36] I. Zagorodnov, T. Weiland, and M. Dohlus, *Wake fields generated by the LOLA-IV structure and the 3rd harmonic section in TTF-II*, Tech. Rep. TESLA Report 2004-01 (DESY, Darmstadt, Germany, 2004).
- [37] F.-A. Fortin, F.-M. De Rainville, M.-A. Gardner, M. Parizeau, and C. Gagné, DEAP: Evolutionary algorithms made easy, *Journal of Machine Learning Research* **13**, 2171 (2012).
- [38] T. Charles, M. Boland, R. Dowd, and D. Paganin, Beam by Design: Current Pulse Shaping Through Longitudinal Dispersion Control, in *Proc. of International Particle Accelerator Conference (IPAC'17), Copenhagen, Denmark, 14-19 May, 2017*, International Particle Accelerator Conference No. 8 (JACoW, Geneva, Switzerland, 2017) pp. 644–647, <https://doi.org/10.18429/JACoW-IPAC2017-MOPIK055>.
- [39] R. J. England, J. B. Rosenzweig, G. Andonian, P. Musumeci, G. Travish, and R. Yoder, Sextupole correction of the longitudinal transport of relativistic beams in dispersionless translating sections, *Phys. Rev. ST Accel. Beams* **8**, 012801 (2005).
- [40] T. Xu, C. Jing, A. Kanareykin, P. Piot, and J. Power, Optimized electron bunch current distribution from a radiofrequency photo-emission source, in *Proc. 2018 IEEE Advanced Accelerator Concepts Workshop (AAC)* (2018) pp. 1–5.
- [41] K. Floettmann, *ASTRA – A Space Charge Tracking Algorithm* (Deutsches Elektronen-Synchrotron, Hamburg, Germany, 2017).
- [42] J. Bisognano, R. Bosch, D. Eisert, M. Fisher, M. Green, K. Jacobs, K. Kleman, J. Kulpin, G. Rogers, J. Lawler, D. Yavuz, and R. Legg, *Progress Toward the Wisconsin Free Electron Laser*, Tech. Rep. (Jefferson Lab, 2011) JLAB-ACC-11-1333.
- [43] J. Bisognano, M. Bissen, R. Bosch, M. Efremov, D. Eisert, M. Fisher, M. Green, K. Jacobs, R. Keil, K. Kleman, G. Rogers, M. Severson, D. D Yavuz, R. Legg, R. Bachimanchi, C. Hovater, T. Plawski, and T. Powers, Wisconsin SRF Electron Gun Commissioning, in *Proceedings of the 25th Particle Accelerator Conference, PAC 2013* (2013) p. 622.
- [44] R. Legg, W. Graves, T. Grimm, and P. Piot, Half wave injector design for WiFEL, in *EPAC 2008 - Contributions to the Proceedings* (European Physical Society Accelerator Group (EPS-AG), 2008) pp. 469–471.

- [45] W. H. Tan, P. Piot, and A. Zholents, Longitudinal-Phase-Space Manipulation for Efficient Beam-Driven Structure Wakefield Acceleration, in *Proc. 10th International Particle Accelerator Conference (IPAC'19), Melbourne, Australia, 19-24 May 2019*, International Particle Accelerator Conference (JACoW Publishing, Geneva, Switzerland, 2019) pp. 2296–2299, issue: 10.
- [46] G. Nielsen, N. Hauge, E. Krauthammer, and A. Bau-richter, Compact high-Tc 2G superconducting solenoid for superconducting RF electron gun, in *Proc. 4th International Particle Accelerator Conference (IPAC2013), Shanghai, China, 12-17 May, 2013* (JACoW, Geneva, Switzerland, 2020) pp. 3514–3516.
- [47] T. Xu, C.-J. Jing, A. Kanareykin, P. Piot, and J. Power, Spatio-Temporal Shaping of the Photocathode Laser Pulse for Low-Emittance Shaped Electron Bunches, in *Proc. 10th International Particle Accelerator Conference (IPAC'19), Melbourne, Australia, 19-24 May 2019*, International Particle Accelerator Conference No. 10 (JACoW Publishing, Geneva, Switzerland, 2019) pp. 2163–2166.
- [48] S. Gilevich, S. Alverson, S. Carbajo, S. Droste, S. Edstrom, A. Fry, M. Greenberg, R. Lemons, A. Miahnahri, W. Polzin, S. Vetter, and F. Zhou, The LCLS-II photo-injector drive laser system, in *Proc. Conference on Lasers and Electro-Optics* (Optical Society of America, 2020) p. SW3E.3.
- [49] G. Ferrini, P. Michelato, and F. Parmigiani, A Monte Carlo simulation of low energy photoelectron scattering in Cs₂Te, *Solid State Communications* **106**, 21 (1998).
- [50] P. Piot, Y.-E. Sun, T. J. Maxwell, J. Ruan, E. Secchi, and J. C. T. Thangaraj, Formation and acceleration of uniformly filled ellipsoidal electron bunches obtained via space-charge-driven expansion from a cesium-telluride photocathode, *Phys. Rev. ST Accel. Beams* **16**, 010102 (2013).
- [51] A. Aryshev, M. Shevelev, Y. Honda, N. Terunuma, and J. Urakawa, Femtosecond response time measurements of a Cs₂Te photocathode, *Applied Physics Letters* **111**, 033508 (2017), <https://doi.org/10.1063/1.4994224>.
- [52] V. Jain and others, 650 MHz Elliptical Superconducting RF Cavities for PIP-II Project, in *Proceedings, 2nd North American Particle Accelerator Conference (NAPAC2016): Chicago, Illinois, USA, October 9-14, 2016* (2017) p. WEB3CO03.
- [53] S. D. Mitri and M. Cornacchia, Transverse emittance-preserving arc compressor for high-brightness electron beam-based light sources and colliders, *EPL (Europhysics Letters)* **109**, 62002 (2015).
- [54] J. A. G. Akkermans, S. Di Mitri, D. Douglas, and I. D. Setija, Compact compressive arc and beam switchyard for energy recovery linac-driven ultraviolet free electron lasers, *Phys. Rev. Accel. Beams* **20**, 080705 (2017).
- [55] S. D. Mitri, Bunch Length Compressors, in *Proceedings of the CAS-CERN Accelerator School on Free Electron Lasers and Energy Recovery Linacs*, Vol. 1 (CERN, Geneva, Switzerland, 2018) p. 363.
- [56] A. Chao, K. H. Mess, M. Tigner, and F. Zimmermann, *Handbook of Accelerator Physics and Engineering*, 2nd ed. (WORLD SCIENTIFIC, 2013).
- [57] D. Robin, E. Forest, C. Pellegrini, and A. Amiry, Quasi-isochronous storage rings, *Phys. Rev. E* **48**, 2149 (1993).
- [58] P. H. Williams, G. Pérez-Segurana, I. R. Bailey, S. Thorin, B. Kyle, and J. B. Svensson, Arclike variable bunch compressors, *Physical Review Accelerators and Beams* **23**, 100701 (2020).
- [59] E. Saldin, E. Schneidmiller, and M. Yurkov, Longitudinal space charge-driven microbunching instability in the TESLA test facility linac, *Nucl. Instrum. Methods Phys. Res., Sect. A* **528**, 355 (2004), also in Proc. 25th International Free Electron Laser Conference, and the 10th FEL Users Workshop.
- [60] Z. Huang, M. Borland, P. Emma, J. Wu, C. Limborg, G. Stupakov, and J. Welch, Suppression of microbunching instability in the linac coherent light source, *Phys. Rev. ST Accel. Beams* **7**, 074401 (2004).
- [61] Y. S. Derbenev, J. Rossbach, E. L. Saldin, and V. D. Shiltsev, *Microbunch radiative tail - head interaction*, Tech. Rep. TESLA-FEL 1995-05 (DESY, 1995) series: TESLA-FEL Reports.
- [62] G. Huang *et al.*, High Precision RF Control for the LCLS-II, in *Proc. 3rd North American Particle Accelerator Conference (NAPAC'16), Chicago, IL, USA, October 9-14, 2016*, North American Particle Accelerator Conference No. 3 (JACoW, Geneva, Switzerland, 2017) pp. 1292–1296, <https://doi.org/10.18429/JACoW-NAPAC2016-FRA2IO02>.
- [63] T. A. Mohayai, P. Snopok, D. Neuffer, and C. Rogers, Novel Application of Density Estimation Techniques in Muon Ionization Cooling Experiment, in *Proceedings, Meeting of the APS Division of Particles and Fields (DPF 2017): Fermilab, Batavia, Illinois, USA, July 31 - August 4, 2017* (2017).
- [64] J. Qiang, R. D. Ryne, M. Venturini, A. A. Zholents, and I. V. Pogorelov, High resolution simulation of beam dynamics in electron linacs for x-ray free electron lasers, *Phys. Rev. ST Accel. Beams* **12**, 100702 (2009).
- [65] E. L. Saldin, E. A. Schneidmiller, and M. V. Yurkov, On the coherent radiation of an electron bunch moving in an arc of a circle, *Nucl. Instrum. Methods Phys. Res., Sect. A* **398**, 373 (1997).
- [66] C. E. Mitchell, J. Qiang, and R. D. Ryne, A fast method for computing 1-D wakefields due to coherent synchrotron radiation, *Nucl. Instrum. Methods Phys. Res., Sect. A* **715**, 119 (2013).